

Cross-Modal Causal Intervention for Medical Report Generation

Weixing Chen, Yang Liu, *Member, IEEE*, Ce Wang, Jiarui Zhu, Shen Zhao, Guanbin Li, *Member, IEEE*, and Liang Lin, *Fellow, IEEE*

Abstract—Medical report generation (MRG) is essential for computer-aided diagnosis and medication guidance, which can relieve the heavy burden of radiologists by automatically generating the corresponding medical reports according to the given radiology image. However, due to the spurious correlations within image-text data induced by visual and linguistic biases, it is challenging to generate accurate reports reliably describing lesion areas. Moreover, the cross-modal confounders are usually unobservable and challenging to be eliminated explicitly. In this paper, we aim to mitigate the cross-modal data bias for MRG from a new perspective, i.e., cross-modal causal intervention, and propose a novel Visual-Linguistic Causal Intervention (VLCI) framework for MRG, which consists of a visual deconfounding module (VDM) and a linguistic deconfounding module (LDM), to implicitly mitigate the visual-linguistic confounders by causal front-door intervention. Specifically, due to the absence of a generalized semantic extractor, the VDM explores and disentangles the visual confounders from the patch-based local and global features without expensive fine-grained annotations. Simultaneously, due to the lack of knowledge encompassing the entire field of medicine, the LDM eliminates the linguistic confounders caused by salient visual features and high-frequency context without constructing a terminology database. Extensive experiments on IU-Xray and MIMIC-CXR datasets show that our VLCI significantly outperforms the state-of-the-art MRG methods. The code and models are available at <https://github.com/WissingChen/VLCI>.

Index Terms—Medical report generation, causality, visual-language pre-training model.

I. INTRODUCTION

MEDICAL images (e.g., X-Ray, MRI) are widely used in clinical procedures [1], providing significant evidence for disease analysis and medical diagnosis [2]. Nevertheless, observing suspicious lesions and writing a coherent diagnosis report is time-consuming, even for experienced radiologists. Furthermore, inexperienced radiologists often fail to capture

This work is supported in part by the National Key R&D Program of China under Grant No.2021ZD0111601, in part by the National Natural Science Foundation of China under Grant No.62002395 and No.61976250, in part by the Guangdong Basic and Applied Basic Research Foundation under Grant No.2023A1515011530, No.2021A1515012311 and No.2020B1515020048, and in part by the Guangzhou Science and Technology Planning Project under Grant No. 2023A04J2030. (Corresponding author: Yang Liu.)

Weixing Chen, Yang Liu, Guanbin Li and Liang Lin are with the School of Computer Science and Engineering, Sun Yat-sen University, China. (E-mail: chen867820261@gmail.com, liuy856@mail.sysu.edu.cn, liguanbin@mail.sysu.edu.cn, linliang@ieee.org)

Ce Wang is with the Key Lab of Intelligent Information Processing of Chinese Academy of Sciences (CAS), Institute of Computing Technology, CAS, Beijing, China. (E-mail: fogever@icloud.com)

Jiarui Zhu is with the Hong Kong Polytechnic University. (E-mail: jiarui.zhu@connect.polyu.hk)

Shen Zhao is with the School of Intelligent Systems Engineering, Sun Yat-sen University, China. (E-mail: z-s-06@163.com)

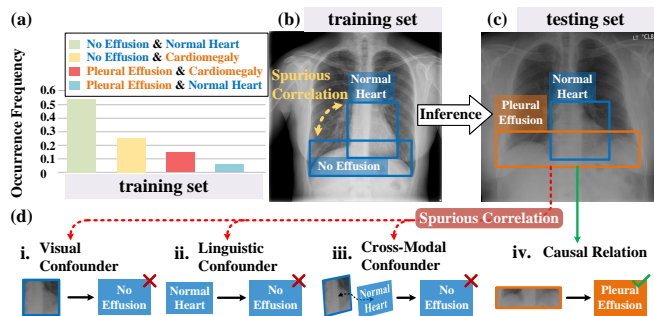


Fig. 1. The example of visual-linguistic spurious correlation of MRG, where the tags (e.g., “No Effusion”, “Normal Heart”) represent different findings, and the boxes represent their regions. Blue color means normal findings while orange means abnormal ones. (a) illustrates the combinations of cardiac enlargement and chest effusion findings, along with their distribution in the training dataset, with the majority representing normal cases. This data bias also results in (b) showcasing spurious correlation, leading to a reliance on spurious correlation for inference in (c). In (d), these spurious correlations encompass three scenarios, namely visual confounders, linguistic confounders, and cross-modal confounders. In this context, visual confounders can be regarded as visual features related to the cardiac region, linguistic confounders pertain to descriptions of a normal heart, and cross-modal confounders arise due to the emphasis on visual features of the cardiac region, leading to wrong judgments. Actually, we encourage the model to focus on chest features (true causal relation) when assessing the presence of chest effusion.

tiny abnormalities due to the high requirement for clinical knowledge. To relieve this issue, Medical Report Generation (MRG) has emerged and attracted growing interest in recent years [3]. MRG extracts features from medical images and generates the corresponding reports, which is similar to image captioning [4]. However, the current MRG faces three challenges that are significantly different from the image captioning task: 1) Longer sentence generation (60-100 tokens) tends to accumulate a larger bias, whereas image captions typically consist of fewer than 20 tokens [5]. 2) The necessity to capture all key regions in the medical image (i.e., abnormalities and diagnostic evidence) and a low tolerance for factually incorrect information [3]. 3) More sophisticated linguistic and visual semantic patterns require a proficient understanding of complex medical information, whereas entities in natural images are diverse and easily distinguishable [6], [2]. Therefore, these challenges impose significant limitations on modeling visual-linguistic interactions and learning informative cross-modal representations for accurate MRG [5].

To tackle the aforementioned challenges, current MRG methods have made significant efforts, such as the memory-driven module for longer sentence generation [5], additional knowledge for more accurate description [7], and contrast with normal samples (i.e., images without lesion areas) for the

capture of abnormalities (i.e., lesion areas within images) [8]. Actually, most of the previous MRG methods aim to capture the latent subtle differences in images (visual biases) and learn a concise set of key descriptions in the text (linguistic biases) for accurate long-sequence generation. Moreover, these methods usually focus on training computationally expensive models based on a large number of region-level annotations [3] and task-specific knowledge¹, rather than mitigating cross-modal biases. Nevertheless, significant visual and linguistic biases exist in numerous image-text data, as shown in Fig. 1. Therefore, lightweight models that can mitigate the cross-modal data bias are essential for MRG to accurately discover abnormalities and generate reliable reports.

Moreover, the most significant difficulty in MRG is the existence of visual and linguistic biases that lead to entangled cross-modal features, i.e., spurious correlations, causing the incorrect report in the model prediction with confounders. This means that the complexity of the medical diagnosis requires the discovery of true causal relations rather than spurious correlations, especially for medical diagnosis when considering rare cases. Actually, the majority of samples in medical reports consist of normal individuals, while there are a limited number of abnormal samples that require comprehensively considering various organs to determine pathological changes in other regions. Additionally, there exist significant visual-linguistic biases in the training sets, which makes the MRG model predict wrong reports in the testing set when relying on the spurious correlations in the training set, as shown in Fig. 1(a-b). This indicates the necessity to uncover true causal relations. Otherwise, spurious correlations may be employed, leading to an inaccurate estimation of “No Effusion” instead of “Pleural Effusion”, as shown in Fig. 1(c-d).

To mitigate the visual-linguistic bias, causal inference [10], [11] has shown promising performance in image classification [12], image question answering [13], [14], and image captioning [15]. However, directly applying existing causal methods to the MRG task may yield unsatisfactory results due to the unobservable confounders in the visual and linguistic domain and the complex visual-linguistic interaction in medical images and textual reports. Although back-door intervention can cut off the shortcut path, it requires approximating the observable confounders using a well-trained visual object detector or a well-constructed linguistic dictionary. Fortunately, causal front-door intervention gives a feasible way to calculate unobservable confounders and mitigate visual-linguistic spurious correlations. With causal front-door intervention, we can eliminate the spurious cross-modal correlations effectively by introducing an additional mediator [16], [17] and generate an accurate description of “Pleural Effusion”. The mediator can be assumed as the feature of “Pleural” in different findings (e.g., “Normal Heart”) to estimate the sub-distribution of “Pleural Effusion” [18]. However, the accurate and reasonable acquisition of the mediator is challenging, especially without the support of additional medical knowledge.

Motivated by the effectiveness of causal inference in decon-

founding the cross-modal bias, we propose a lightweight cross-modal causal intervention framework for MRG without the observable confounders assumption, named Visual-Linguistic Causal Intervention (**VLICI**), to mitigate the visual and linguistic data biases. Specifically, we propose Prefix Language Modeling (PLM) and degradation-aware Masked Image Modeling (MIM) for cross-modal pre-training. To mitigate the visual and linguistic biases, we propose the visual deconfounding module (**VDM**) and linguistic deconfounding module (**LDM**) based on the causal front-door intervention paradigm. In VDM, the visual mediator is constructed by local detail information (e.g., lung texture) and global contour (e.g., lung contour) from medical images, to disentangle the visual features. The linguistic confounders can be eliminated by the LDM, which estimates the change in the probability of word embedding caused by visual details and linguistic context. In summary, our main contributions are listed as follows:

- To implicitly mitigate cross-modal biases, we propose visual-linguistic causal front-door intervention modules VDM and LDM based on the Structural Causal Model. The VDM aims to disentangle the region-based features from images, and the LDM aims to eliminate the spurious correlations caused by the visual-linguistic embedding.
- To alleviate the problem of unpaired data and capture detailed features when pre-training cross-modal data, we propose PLM and degradation-aware MIM for pre-training in various data situations (e.g., unpaired, single modality), which is efficient and easy to implement.
- We propose a lightweight Visual-Linguistic Causal Intervention (VLICI) framework for MRG, which introduces mediators without additional knowledge, to implicitly deconfound the visual-linguistic features by causal front-door intervention. To the best of our knowledge, we are the first to conduct cross-modal causal intervention for MRG. Experiments show that we achieve state-of-the-art performance on IU-Xray and MIMIC-CXR datasets.

II. RELATED WORK

A. Image Captioning

Image captioning aims to understand image information and describe it in text, which mainly adopts the encoder-decoder framework [19]. Recent work has achieved significant success in this task, generally improving model performance from three aspects: visual representation learning, linguistic comprehension and generation, and training strategy [20]. The global features extractor from CNNs leads to excessive compression of information and lacks granularity [21], thus, visual saliency can further improve performance via the spatial relation of regional features and rely on the integration of visual and semantic data to improve performance [22], [23], [24]. As for the linguistics features, generating the captioning from coarse to fine [25] and integrating multi-modal information via multiple layers of LSTM [22], [26] achieve a promising performance, but are limited by the training efficiency and expression ability. With the rise of transformer-based models [19], [27], intrinsic information of each modality is learned through self-attention, while cross-attention enables the learning of

¹These methods build the template or knowledge database laboriously, making it hard to transfer those approaches directly to other datasets [9].

multi-modal information, thereby effectively enhancing the model’s performance [28], [15]. Furthermore, the performance improvements can be achieved by the formulation of training strategies, including the learning order of the samples [29], reinforcement learning [30], [4], and visual-linguistic pre-training [31], [32]. Compared with the image captioning approaches, the MRG has similar structures [20]. Nevertheless, image captioning usually generates single sentence to describe the main entities, while the MRG focuses on potential subtle lesion areas in medical images and generates longer sentences from more sophisticated visual-linguistic semantics.

B. Causal Inference

As the visual-linguistic bias caused by the heterogeneity of multi-modal data, causality provides a new methodology to design robust models via the elimination of spurious correlation [33], [34], [11]. Causal inference estimates the hidden causal effects in the distribution while significantly improving the model’s generalization. It mitigates confounders through back-door, front-door intervention, or counterfactual intervention. This approach substantially advances the performance of tasks, including image classification [35], image semantic segmentation [36], visual features representation [37], [38], image captioning [18], [15], and VQA [16]. Specifically, Wang et al. [13] improved Faster R-CNN by causal back-door intervention to obtain a more robust object detection model, which improves the performance of VQA [39] and image captioning [15]. Furthermore, it can also achieve deconfounding by simulating causal interventions based on human priors in modeling [40]. However, the confounders are usually unobservable and elusive, thus front-door intervention and counterfactual intervention can be applied. Specifically, the implicit capture of potential confounders can be achieved by integrating the causal intervention mechanism into the attention module through cross-sample attention or self-annotation [41], [17], [38], [42]. Additionally, Liu et al. proposed event-level causal visual question answering utilizing visual front-door intervention, which uses attention to aggregate local and global causality-aware visual-linguistic representations [16]. Therefore, causal inference has achieved remarkable performance in cross-modal tasks [11]. Compared with the previous works that address VQA or image captioning, we focus on a more challenging task MRG, which requires modeling complex visual-linguistic interaction in medical images and textual reports [43], [44], [45]. And we propose a visual-linguistic front-door causal intervention that simultaneously eliminates spurious correlations from visual and linguistic confounders.

C. Medical Report Generation

Recently, MRG methods have followed the works of image captioning and have shown remarkable performance. However, the abnormal descriptions and lesion regions in patient samples only constitute a small portion, leading to the visual-linguistic bias in the MRG task. To address this issue, knowledge-aware methods prevail because they can explore and distill the knowledge to accurately identify abnormalities and describe them using appropriate terminology. Specifically, the

bias from language can be mitigated by utilizing the general graph [6] as prior knowledge [7], [46], [47]. However, fixed and limited knowledge is insufficient to address complex medical problems. Therefore, Yang et al. [9] and Li et al. [48] employed RadGraph [49] for knowledge retrieval and dynamic knowledge construction. Additionally, utilizing a well-trained label extractor or manually annotated region labels for classification tasks, and further incorporating them to assist in report generation, can also be considered as approaches leveraging external knowledge [50], [51], [3]. Although the knowledge-based model is a promising direction, acquiring knowledge is expensive and challenging to transfer to other tasks. Therefore, CA [8] and CMCL [52] explored the potential abnormal regions by comparing them with normal samples. Moreover, knowledge can be retrieved or constructed using templates corresponding to similar images [9], [48], which effectively mitigates the issue of representation distortion caused by excessive focus on knowledge. Additionally, the template-based approach requires several samples for comparison, memory-driven transformers can implicitly store the visual [53], [54] and linguistic [5] context without templates. However, considering only the context would lead to cross-modal bias. Thus, the models align the cross-modal information in the embedding space and incorporate it as memory, which can be retrieved by visual-linguistic features [55], [51]. The visual-linguistic bias hinders the robustness and reliability of MRG. To mitigate the cross-modal bias, we introduce a lightweight VLCI approach that implicitly mitigates cross-modal confounders, uncovers the true cross-modal causality through causal front-door intervention, and reduces the need for additional annotation when discovering abnormalities.

III. METHOD

In this section, we first introduce the visual-linguistic pre-training (VLP), followed by the two essential cross-modal causal intervention modules, i.e., the Visual Deconfounding Module (VDM) and the Linguistic Deconfounding Module (LDM). Then, we introduce how to integrate VDM and LDM into the VLCI for cross-modal causal intervention.

A. Overview

A typical MRG model can generate a series of medical findings and insights given a medical image. As shown in Fig. 2, upon receiving the Chest X-ray image $I \in \mathbb{R}^{C \times H \times W}$, the VLCI first utilizes a visual feature extractor to obtain h_v , which guides the generation of the next word $w_i \in R$ from the prefix text embedding h_w . However, due to the presence of confounders Z in both the visual and linguistic modalities, the non-causal model may capture the spurious correlations between “Normal Heart” and “No Effusion”, which causes the neglect of “Pleural Effusion” accompanied by “Normal Heart”, as shown in Fig. 2(a). Fortunately, the SCM of VLCI in Fig. 2(a), which shows the link between Z and F can be cut off by the mediators. The existence of mediators enables the intervention and adjustment of the relation between F and R , thereby revealing the true causal relation between the two variables. Thus, we perform a causal

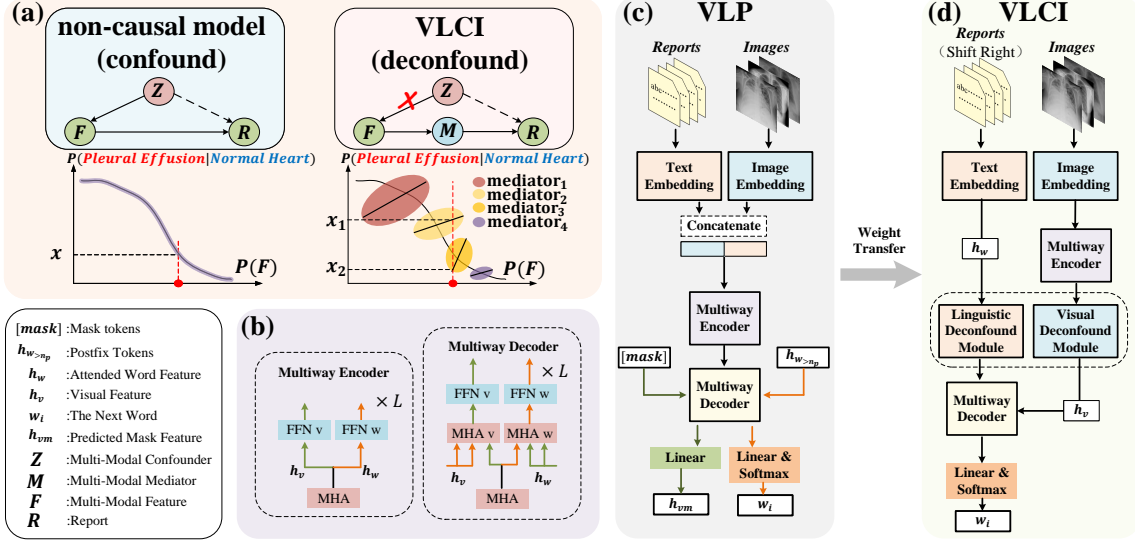


Fig. 2. The mechanism of front-door causal intervention via the structural causal model (SCM) (a) is implemented in the example from Fig. 1, in contrast to the non-causal model. Our approach follows a two-stage pipeline: 1) Visual Linguistic Pre-training (VLP) (c) utilizes the Multiway Transformer (b) to learn multi-modal context and concepts, and achieve effective cross-modal alignment. 2) Visual-Linguistic Causal Intervention (VLCI) (d) consists of a pre-trained transformer, a Visual Deconfounding Module (VDM), and a Linguistic Deconfounding Module (LDM), which is implemented after VLP to mitigate the cross-modal bias. The image embedding module employs the initial three blocks of ResNet101. Specifically, the VDM explores visual bias using local sampling and global sampling. The LDM estimates linguistic bias using a vocabulary dictionary and visual features.

intervention on the multi-modal feature prior to the decoder to estimate the deconfounded probability of the correct word. This estimation is achieved by aggregating the probabilities of each sub-distribution of mediators, as illustrated in Fig. 2(a). Nevertheless, due to the absence of elaborate datasets and a well-trained feature extractor, we conduct a causal front-door intervention to eliminate the spurious correlations via mediator M implicitly. However, the estimation of both confounders and the mediator requires sufficient prior information, i.e., various visual-linguistic concepts. Therefore, we leverage the Visual-Language Pre-training (VLP) model to construct the correlation between the visual contexts and linguistic concepts before conducting the causal intervention.

B. Visual-Linguistic Pre-training (VLP)

In the medical pre-training framework, there exist two difficulties: (1) the unpaired data that only has a single modality is hard to be utilized in supervised learning, and (2) heterogeneous data that makes it difficult to distinguish the region features because the morphology of the same lesion varies greatly [2]. To address these challenges and provide fine-grained region features without region labels, we employ a cross-modal pre-training approach to learn and align multi-modal information [56], as shown in Fig. 2(c). For language concepts, we employ Prefix Language Modeling (PLM) to align with the visual modality utilizing bidirectional attention in image and prefix text. Meanwhile, to acquire visual context, we utilize Masked Image Modeling (MIM) for pixel-level semantic learning. Additionally, to capture more detailed features, we utilize degradation of the image and masking the features extracted by CNN. Therefore, we use a multiway transformer to extract multi-modal features and two linear layers to solve PLM and MIM tasks, respectively [32], [57]. In each block of the multiway encoder, the attention layer

is weight-shared while the two feed-forward layers handle the corresponding modal features respectively [58]. Similarly, each block of the multiway decoder consists of a weight-shared self-attention layer, a pool of feed-forward networks used for different modalities, as shown in Fig. 2(b).

1) *PLM*: Motivated by the work of SimVLM [32], we extract image features from the first three blocks of ResNet101 [59] as prefix tokens in the PLM. Simultaneously, the text is randomly divided into two parts, with one part generated by another under the guidance of the obtained image tokens. In cases where the corresponding image is missing, the PLM can still be trained using only the text, similar to SimVLM. Let $h_v \in \mathbb{R}^{\frac{H \times W}{P^2} \times d}$ denote the image token extracted from the raw image I , where P represents the patch size and d is the embedding size. Then, $\{w_{np}, \dots, w_n\}$ represents the postfix sequence following the textual description h_w of length $n_p \geq 0$. Thus, the formulation is as follows:

$$\mathcal{L}_{\text{PLM}}(\theta) = - \sum_{i=n_p}^n \log P_{\theta}(w_i | h_v, h_{w_{<n_p}}), \quad (1)$$

Here, θ denotes the trainable parameters of the model, h_v represents the visual embedding with a trainable 2D positional encoding, h_w is learned based on a fixed vocabulary and serves as the prefix received by the encoder, and n denotes the length of the report.

2) *MIM*: To handle unpaired images, we leverage the Masked Image Modeling (MIM) paradigm [57]. Furthermore, since MIM can be trained using pairwise data [60], the missing semantics of masked images can be complemented by text, thereby enhancing cross-modal association. Additionally, we learn medical image representations by reconstructing high-resolution patches from low-resolution inputs, which can encode more local information into latent embeddings [61]. Consequently, we sub-sample the images for degradation be-

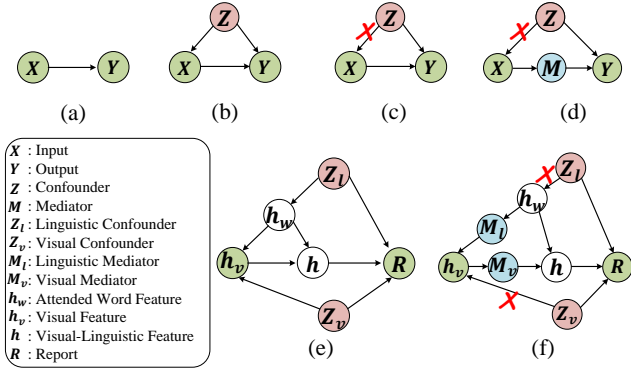


Fig. 3. The structural causal model (SCM) depicted in (a) shows that Y is caused by X . However, when two or more variables or events are influenced by a common cause, it leads to a spurious correlation, involving confounders Z as shown in (b). In (c), the back-door causal intervention is demonstrated to calculate the probabilities of observable confounders Z , effectively blocking the back-door path $Z \rightarrow X$, and obtaining the true probability of Y . Furthermore, when dealing with unobservable confounders, the front-door causal intervention can estimate the mediator M and subsequently block the path $Z \rightarrow X \rightarrow M$. In our proposed approach (e), we decompose the cross-modal confounders into visual (Z_v) and linguistic (Z_l) components. The front-door causal intervention is implemented by the mediators M_v and M_l , effectively blocking the paths $Z_v \rightarrow h_v$ and $Z_l \rightarrow h_w$, thereby preventing the back-door paths $h_v \leftarrow Z_v \rightarrow R$ and $h_v \leftarrow h_w \leftarrow Z_l \rightarrow R$. Finally, the structural causal model (SCM) of VLCI is obtained, as depicted in (f).

fore the visual embedding and reconstruct the masked visual token extracted from CNNs by incorporating the semantics of both the unmasked visual token and the linguistic token. This approach enables us to capture subtle differences in the dataset [62]. The objective of MIM can be formulated as:

$$\mathcal{L}_{\text{MIM}}(\theta) = P_{\theta}(h_{vm}|h_{vv}, h_w), \quad (2)$$

where h_{vm} represents the masked visual tokens extracted by the ResNet backbone, h_{vv} refers to the unmasked tokens, and h_w corresponds to the word tokens of the entire report.

C. Visual-Linguistic Causal Intervention

After the Visual-Linguistic pre-training (VLP), the learned visual-linguistic feature encoders still contain visual and linguistic biases from cross-modal confounders [18]. Therefore, we further employ front-door causal intervention to discover the causal effect between visual and linguistic modalities during MRG, as shown in Fig. 2(d).

1) *Preliminaries*: To clarify the mechanism of causal intervention, we introduce Pearl’s Structural Causal Model (SCM) [33], as shown in Fig. 3. The SCM is a mathematical framework used in causal inference to model the relations among variables and determine cause and effect relations. The SCM uses directed acyclic graphs (DAGs) to represent causal systems, where each variable is a node and the arrows represent causal relations between the variables.

In Fig. 3(a), the chain structure $X \rightarrow Y$ represents the output Y is affected by the input X , formulated as $P(Y|X)$. But the confounders Z caused by data bias would lead to a spurious correlation, as shown in Fig. 3(b). This graph indicates that two causes (both X and Z) lead to the common effect or outcome (Y), such as the cross-modal confounders of “Normal Heart” and cross-modal feature of “Pleural” leading

to a confounded estimation of “No Effusion” (the spurious correlation is “Normal Heart” and “No Effusion”). In this case, we formulate $P(Y|X)$ as:

$$P(Y|X) = \sum_z P(Y|X, Z = z)P(Z = z|X), \quad (3)$$

where the confounders Z generally brings about the observational bias via $P(z|X)$ [15]. To alleviate this issue, back-door causal intervention can be implemented by introducing the do calculus $do(\cdot)$ [15], [16], [63], [64]. We can calculate the probabilities of observable confounders and block the back-door path $Z \rightarrow F$, the interventional probability is as follows:

$$P(Y|do(X)) = \sum_z P(Y|X, Z = z)P(Z = z), \quad (4)$$

where Z can be the learned RoI features of the heart and the attended word feature of “Normal Heart”. However, the back-door causal intervention is limited by the observability of confounders, and the front-door causal intervention provides an implicit method of deconfounding in Fig. 3 (d). To eliminate the unobservable confounder, we introduce the mediator M to cut off the link $X \leftarrow Z \rightarrow Y$. The total probability $P(Y|do(X))$ can be represented as the following summation:

$$P(Y|do(X)) = \sum_m P(Y|do(X), M = m)P(M = m|do(X)), \quad (5)$$

where M is introduced by X without the back-door path. Thus, the intervention probability is equal to the conditional probability in the path $X \rightarrow M$ [16]. Besides, there is no direct causal path between X and Y . In this way, the introduced summation in Eq. (5) can be reformulated as:

$$\begin{aligned} P(Y|do(X)) &= \sum_m P(Y|do(X), do(M = m))P(M = m|X = x) \\ &= \sum_m P(Y|do(M = m))P(M = m|X = x). \end{aligned} \quad (6)$$

To estimate $P(Y|do(M = m))$, we can apply the back-door intervention to cut off the link $M \leftarrow X \leftarrow Z \rightarrow Y$ [15]. Therefore, we have the intervention probability formulation:

$$\begin{aligned} P(Y|do(M = m)) &= \sum_{\hat{x}} P(Y|do(M = m), X = \hat{x})P(X = \hat{x}|do(M = m)) \\ &= \sum_{\hat{x}} P(X = \hat{x})P(Y|X = \hat{x}, M = m), \end{aligned} \quad (7)$$

where \hat{x} is the selected features from X not caused by M . Finally, we can calculate Eq. (6) by applying Eq. (7):

$$P(Y|do(M = m)) = \sum_m P(M = m|X = x) \sum_{\hat{x}} P(X = \hat{x})P(Y|X = \hat{x}, M = m). \quad (8)$$

However, existing front-door causal intervention methods employ diverse approaches for estimating mediators and conducting interventions. In MRG, we construct the structural causal model (SCM) similar to Image Caption [15], assuming

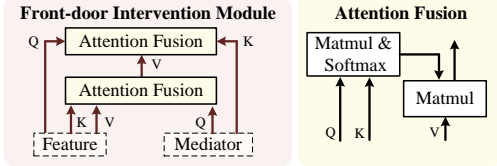


Fig. 4. Illustration of the Front-door Intervention Module (FIM), which consists of two Attention Fusion layers with non-parameters.

that h_v is the visual feature, h_w is the linguistic feature of the attended word, and h is the fusion feature from h_v and h_w ($h_v \rightarrow h \leftarrow h_w$), leading to the generation of report R . Moreover, h_v would be influenced by h_w through cross-attention and makes $h_v \leftarrow h_w$, as shown in Fig. 3 (e). Following that, we divide the mediator into visual and linguistic modalities and introduce a Front-door Intervention Module (FIM) based on Equation (8) to deconfound them.

2) *Front-door Intervention Module (FIM)*: In Fig. 3 (e), the causal effects $h_v \rightarrow R$ and $h_w \rightarrow R$ are affected by the confounders $Z = \{Z_v, Z_l\}$ from back-door paths $h_v \leftarrow Z_v \rightarrow R$ and $h_w \leftarrow Z_l \rightarrow R$ [15], respectively. In our SCM, the non-interventional prediction can be expressed as:

$$\begin{aligned} P(R|I) &= P(R|h_v, h_w) \\ &= \sum_{i=1}^n \sum_z P(w_i|h_v, h_w, Z=z)P(Z=z|h_v, h_w), \end{aligned} \quad (9)$$

where Z brings the spurious correlation via $P(Z=z|h_v, h_w)$, leading to incorrect reports. h_v is the visual token from visual embedding, and h_w is the linguistic token of the attended word from linguistic embedding. Taking Fig. 1 as an example, when $P(Z = \text{“Normal Heart”}|h_v = \text{“Heart”}, h_w = \text{“Normal”})$ is large while $P(Z = \text{“Cardiomegaly”}|h_v = \text{“Heart”}, h_w = \text{“Normal”})$ is small in the training set, it tends to enlarge $P(R = \text{“No Effusion”}|h_v, h_w, Z = \text{“Normal Heart”})$ in the testing set. To mitigate visual-linguistic confounders and uncover the true causal structure, we apply causal front-door intervention by introducing mediator M_v and M_l , respectively, as shown in Fig. 3 (f). Generally, Z_v is unobservable without a well-trained object detector, and the back-door path $h_v \leftarrow Z_v \rightarrow R$ can be blocked by M_v via learning the true causal effect $h_v \rightarrow M_v \rightarrow h \rightarrow R$. Similarly, the intervention on the back-door path $h_v \leftarrow h_w \leftarrow Z_l \rightarrow R$ can be implemented by calculating the M_l without well-constructed confounders dictionaries. Thus, we can formulate Eq. (9) as:

$$P(R|do(I)) = P(R|do(h_v), do(h_w)) \quad (10)$$

To further estimate Eq. (10) with the deep learning framework using Eq. (8), we adopt Normalized Weighted Geometric Mean (NWGM) [65] as:

$$P(R|do(h_v), do(h_w)) \approx \text{Softmax}(g(h_w, h_v, \hat{M}_v, \hat{M}_l)). \quad (11)$$

where $g(\cdot)$ denote the network mapping functions, \hat{M}_v and \hat{M}_l denote the estimations of M_v and M_l via VDM and LDM. In Fig. 4, the FIM consists of two Attention Fusion layers and it is integrated into VDM and LDM. Different from the cascaded transformer [28], FIM does not have optimized parameters. It relies on extracted features and intervenes using estimated mediators of the corresponding modalities. This

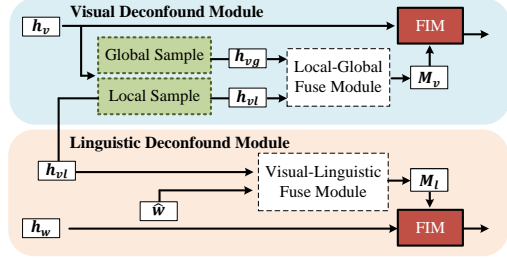


Fig. 5. Illustration of the Visual Deconfounding Module (VDM) and linguistic Deconfounding Module (LDM).

approach ensures that the estimation of mediators is entirely dependent on the sampling in VDM and LDM rather than FIM, achieving implicit learning of mediators.

3) *Visual Deconfounding Module (VDM)*: In Fig. 5, the visual mediator M_v is calculated using local features h_{vl} obtained from local sampling and global features h_{vg} obtained from global sampling. The features h_{vl} represent local details acquired from Local Sampling, while h_{vg} represents contour and position features obtained from Global Sampling [66]. For example, the contour of the heart influences the determination of pleural effusion, and the texture of the lungs can also serve as a basis for detection.

Local Sampling. Inspired by TransFG [67], we leverage the attention accumulated from the encoder to select the top k tokens. These selected visual tokens with high attention correspond to the report’s keywords as $h_{vl} \in \mathbb{R}^{k \times d}$, where $k = 6$ for each attention head, and d is the dimension of the transformer. Subsequently, h_{vl} is further enhanced using CaaM [38], which excavates the local internal relations. Specifically, in CaaM, these highly attended tokens are computed not only with self-attention but also with negative attention scores, aiming to achieve more robust features. The purpose of h_{vl} is to capture crucial local details in the image, which serve as the key basis for further processing.

Global Sampling. The global sampling is implemented by Down Sampling Transformer block, in which the 14×14 visual tokens are down-sampled to 7×7 as $h_{vg} \in \mathbb{R}^{49 \times d}$. Max pooling in this block can better retain the global structure information in the image as the general features of the data itself. We formulate the operation as follows:

$$h_{vg} = W[P(h_v) + \text{Attn}(P(\text{LN}(h_w)))], \quad (12)$$

where P is the 2d max pooling layer, LN is layer normalization, Attn is the 2d relative attention [68], and W denotes the weights of the linear layer.

Local-Global Fuse Module. Finally, the h_{vl} is integrated with h_{vg} to enhance local details with global structural information via Local-Global Fuse Module formulated as Eq. (13), namely mediator M_v .

$$M_v = \text{FFN}([\text{MHA}(h_{vl}, h_{vl}, h_{vl}), \text{MHA}(h_{vl}, h_{vg}, h_{vg})]) \quad (13)$$

where MHA and FFN are the Multi-Head Attention layer and Feed-Forward Network layer, respectively. $[\cdot, \cdot]$ denotes concatenation.

4) *Linguistic Deconfounding Module (LDM)*: For linguistic deconfounding, we have some observations from $h_v \leftarrow h_w \leftarrow$

TABLE I

THE DETAILS OF VLCI AND SEVERAL COMPARED RRG MODELS, THE #ENC AND #DEC DENOTE THE NUMBER OF TRANSFORMER LAYERS IN THE ENCODER AND DECODER, RESPECTIVELY. THE MARKER ♣ MEANS 2 CONTRASTIVE ATTENTIONS, AND ♠ MEANS HIERARCHICAL LSTM. THE BACKBONE OF VLCI IS THE FIRST THREE BLOCKS OF RESNET101.

BESIDES, WE SHOW THE EMPLOYED MODEL BOOSTING MODULES, INCLUDING THE KNOWLEDGE-AWARE MODULE \mathcal{K} , TEMPLATE RETRIEVAL MODULE \mathcal{T} , AND MEMORY-DRIVE MODULE \mathcal{M} . ADDITIONALLY, WE ADOPT TWO SCALES OF THE VLCI, **VLCI₃** FOR THE IU-XRAY DATASET AND **VLCI₆** FOR THE MIMIC-CXR DATASET.

Method	Visual Embedding	#Enc	#Dec	\mathcal{K}	\mathcal{T}	\mathcal{M}
Light	R2Gen[5]	Resnet101	3	3		✓
	R2GenCMN[55]	Resnet101	3	3		✓
	CMCL[52]	Resnet50	/	♠		
	PPKED[7]	Resnet152	2	1	✓	✓
	CA[8]	Resnet50	♣	♠		✓
	AlignTransformer[50]	Resnet50	3	3	✓	✓
	MMTN[70]	DenseNet121	3	3	✓	✓
	Heavy	M2TR[53]	Densenet151	6	12	
MGSK[9]		Resnet101	12	3	✓	✓
RAMT[71]		DenseNet121	6	6	✓	✓
DCL[48]		ViT Linear Projection	25	1	✓	✓
VLCI₃		Resnet101*	3	3		
VLCI₆	Resnet101*	6	6			

$Z_l \rightarrow R$ (Fig. 3 (e)): (1) the linguistic contexts can affect the generation of the next word, and (2) the attended word features affect the attended visual features via cross-attention [15]. Additionally, the difference in word frequency brings a large distance deviation in embedding space, so the distance of word vectors cannot represent semantic relevance well [69].

Visual-Linguistic Fuse Module. Thus, we calculate the linguistic mediator M_l in embedding space via all vocabularies from the tokenizer as the global features and use h_{vl} obtained from the VDM, which estimates the current word frequency to adjust the distribution of h_w , see in Fig. 5.

$$\begin{aligned} h'_{vl} &= \text{FFN}(\text{MHA}(h_{vl}, \hat{w}, \hat{w})); \\ M_t &= \text{FFN}(\text{MHA}(h'_{vl}, h_{vl}, h_{vl})) \end{aligned} \quad (14)$$

where \hat{w} denotes all word tokens from the tokenizer. Then, we build the causal effect $h_w \rightarrow M_l \rightarrow h_v \rightarrow M_v \rightarrow h \rightarrow R$ to cut off the back-door path $h_v \leftarrow h_w \leftarrow Z_l \rightarrow R$ via M_l .

In Fig. 2, the deconfounded visual and linguistic features are fed to the decoder to learn fused cross-modal features. The output layer is a linear projection with softmax operation, mapping probability into the dimensional equal to the vocabulary size. Finally, the training target is to minimize the negative log-likelihood loss according to Eq. (10) and Eq. (11):

$$\mathcal{L}_{\text{nil}}(\theta) = - \sum_{i=1}^n \log(\text{Softmax}(g(h_{w_{<i}}, h_v, \hat{M}_v, \hat{M}_l))) \quad (15)$$

where n is the length of the report and $h_{w_{<i}}$ is the prefix text when estimating the word w_i .

IV. EXPERIMENT

A. Experimental settings

1) **Dataset:** **IU-Xray** [72], also known as the Indiana University Chest X-ray Collection, is a publicly available medical dataset widely used to evaluate the performance of MRG methods. It comprises 7,470 chest images and 3,955 corresponding reports, with an average report length of 30 [46]. To maintain

TABLE II

COMPARISON OF COMPUTATIONAL COST BETWEEN VLCI WITH R2GEN AND R2GENCMN. THE 1st AND 2nd BEST RESULTS ARE BOLDED AND UNDERLINED, RESPECTIVELY.

Method	Inference Time (s)	Params (M)	FLOPs (TFLOPs)	BLEU-4
R2Gen	97.14	78.07	3.66	0.103
R2GenCMN	40.25	58.65	12.98	0.105
VLCI	<u>97.10</u>	<u>69.41</u>	<u>10.50</u>	0.119

consistency, we follow the setting used in R2Gen [5] and partition the dataset into training, validation, and testing sets at a ratio of 7:1:2, ensuring that there is no overlap in patients. We tokenize the words with more than 3 occurrences and set the max length as 60. Note that we adopt two images (frontal and lateral views) as input for each sample.

MIMIC-CXR [73] is a large-scale chest medical dataset, with 377,110 images and 227,835 corresponding reports, of which the average length of reports is 48 in the training/val set and 61 in testing set [46]. We use the official paradigm, the dataset is divided into the training set with 368,960 images and 222,758 reports, the validation set with 2,991 images and 1,808 reports, and the testing set with 5,159 images and 3,269 reports. Different from the IU-Xray dataset, MIMIC-CXR has instances of a single modality (only image or report) as well as multiple images corresponding to one report. Therefore, we use a single image as the input and tokenize the words with more than 10 occurrences, and set the max length as 80.

2) **Baseline Models:** We compare the proposed VLCI model with several state-of-the-art MRG models, including R2Gen [5], R2GenCMN [55], CMCL [52], PPKED [7], CA [8], AlignTransformer [50], M2TR [53], RAMT [71], MMTN [70], MGSK [9], and DCL [48]. These models are categorized into lightweight and heavyweight models. The lightweight models comprise no more than 3-layer modules for both the encoder and the decoder, as detailed in Table I. Most of these models incorporate various modules to enhance their performance, such as the knowledge-aware module, template retrieval module, and memory-drive module, which can be computationally expensive. It is important to note that the total parameters of our VLCI are less than the R2Gen, while VLCI is more efficient by eliminating the recursive memory calculation dependency, as shown in Table II.

3) **Evaluation Metrics:** We adopt the widely used natural language generation (NLG) metrics, including BLEU [74], ROUGE-L [75], METEOR [76] and CIDEr [77]. Since the MRG specifically focuses on the abnormality detection accuracy rather than the text fluency and similarity with the real report, we further adopt clinical efficacy (CE) metrics [5], [8], [53], [9]. It is calculated by the labels extracted from CheXpert [78]. Specifically, the extracted positive labels are considered as positives, while the non-positive labels (negative, not mentioned, and uncertain) are treated as negatives. Using this approach, we calculate the micro-precision, micro-recall, and micro-F1 scores between the labels from reference reports and generated reports.

4) **Implementation Settings:** We use the first three blocks of ResNet101 [59] to extract 1,024 feature maps, which are projected into 512 maps of size 14×14 . The dimension of the transformer layers and the number of attention heads are fixed

TABLE III

THE PERFORMANCES OF VLCI AND OTHER METHODS ON IU-XRAY AND MIMIC-CXR DATASETS. THE 1st AND 2nd BEST RESULTS ARE BOLDED AND UNDERLINED, RESPECTIVELY. FOR SOME METHODS, THE RESULTS ARE MISSING AND DENOTED BY A “/”.

Method	BLEU-1	BLEU-2	BLEU-3	BLEU-4	CIDEr	Rouge-L	METEOR	Precision	Recall	F1
IU-Xray Dataset										
R2Gen[5]	0.470	0.304	0.219	0.165	/	0.371	0.187	/	/	/
CMCL[52]	0.473	0.305	0.217	0.162	/	0.378	0.186	/	/	/
PPKED[7]	0.483	0.315	0.224	0.168	0.351	0.376	0.190	/	/	/
CA[8]	0.492	0.314	0.222	0.169	/	0.381	0.193	/	/	/
AlignTransformer[50]	0.484	0.313	0.225	0.173	/	0.379	<u>0.204</u>	/	/	/
M2TR[53]	0.486	0.317	0.232	0.173	/	<u>0.390</u>	0.192	/	/	/
MGSK[9]	0.496	0.327	0.238	0.178	0.382	0.381	/	/	/	/
RAMT[71]	0.482	0.310	0.221	0.165	/	0.377	0.195	/	/	/
MMTN[70]	0.486	0.321	0.232	0.175	0.361	0.375	/	/	/	/
DCL[48]	/	/	/	0.163	<u>0.586</u>	0.383	0.193	/	/	/
VLCI₃(ours)	0.505	0.334	0.245	0.190	0.592	0.394	0.210	/	/	/
MIMIC-CXR Dataset										
R2Gen[5]	0.353	0.218	0.145	0.103	0.149	0.277	0.142	0.333	0.273	0.276
R2GenCMN[55]	0.356	0.219	0.147	0.105	0.152	0.278	0.141	0.334	0.275	0.278
CMCL[52]	0.334	0.217	0.140	0.097	/	0.281	0.133	/	/	/
PPKED[7]	0.360	0.224	0.149	0.106	<u>0.237</u>	0.284	0.149	/	/	/
CA[8]	0.350	0.219	0.152	0.109	/	0.283	0.151	0.352	0.298	0.303
AlignTransformer[50]	0.378	0.235	0.156	0.112	/	<u>0.283</u>	<u>0.158</u>	/	/	/
M2TR[53]	0.378	0.232	0.154	0.107	/	0.272	0.145	0.240	0.428	0.308
MGSK[9]	0.363	0.228	0.156	0.115	0.203	0.284	/	0.458	0.348	0.371
RAMT[71]	0.362	0.229	0.157	0.113	/	0.284	0.153	0.380	0.342	0.335
MMTN[70]	<u>0.379</u>	<u>0.238</u>	<u>0.159</u>	0.116	/	<u>0.283</u>	0.161	/	/	/
DCL[48]	/	/	/	0.109	0.281	0.284	0.150	0.471	0.352	0.373
VLCI₆(ours)	0.400	0.245	0.165	0.119	0.190	0.280	0.150	0.489	0.340	0.401

to 512 and 8, respectively. In the IU-Xray dataset (referred to as VLCI₃), both the encoder and decoder consist of 3 layers, whereas in the MIMIC-CXR dataset (referred to as VLCI₆), both the encoder and decoder comprise 6 layers, as illustrated in Table I. The variation in the number of layers can be attributed to the significantly larger size of the MIMIC-CXR dataset in comparison to the IU-Xray dataset. During pre-training, we utilize a dataset that combines IU-Xray and MIMIC-CXR datasets, resulting in 4,347 unique words. We perform fine-tuning on these two datasets separately with the same tokenizer as VLP. The batch size is set to 64 during pre-training and 16 during fine-tuning. In the pre-training stage, we adopt an image mask rate of 85% for MIM. The VLP is trained using the AdamW optimizer with a warm-up step of 10% of the total training steps, and the peak learning rate is set to 5e-4. The weight decay of the optimizer is set to 1e-2, and the total epochs are set to 30 in pre-training. In the fine-tuning stage, the model is fine-tuned using the Adam optimizer with an initial learning rate of 1e-5 and a weight decay of 5e-5 for 10 epochs on both the IU-Xray and MIMIC-CXR datasets.

B. Quantitative Analysis

1) *NLG Metric*: As shown in Table III, our VLCI outperforms nearly all the MRG methods. Specifically, compared with the lightweight model MMTN [70], VLCI₃ significantly improves the BLEU-1 metric by 1.9% on the IU-Xray dataset. Similarly, when compared with the heavyweight model RAMT [71], VLCI₆ achieves a substantial 3.8% boost in the BLEU-1 metric on the MIMIC-CXR dataset. This significant improvement in the BLEU-1 metric highlights our method’s ability to select words more precisely. Notably, on the IU-Xray dataset, our tokenizer incorporates words from the MIMIC-CXR dataset, leading to even greater estimation challenges. To assess text fluency more effectively, we also

consider the precise match of four consecutive words using the BLEU-4 metric. Our VLCI demonstrates a 1.5% improvement over MMTN on the IU-Xray dataset and a 0.6% improvement over RAMT on the MIMIC-CXR dataset. Notably, the longer descriptions in the MIMIC-CXR dataset present visual-linguistic data bias and significant spurious correlations among multiple words. Our VLCI effectively leverages cross-modal causal intervention to achieve performance improvement.

In contrast to BLEU, Rouge-L focuses more on the structural and sequential similarity of sentences. Our method demonstrates significant superiority on the IU-Xray dataset while exhibiting slightly lower performance compared to DCL [48] on the MIMIC-CXR dataset. However, Table III reveals that all methods achieve Rouge-L scores around 0.280 on the MIMIC-CXR dataset. This observation suggests that, when generating long sentences, the differences in structure and sequence with the reference reports are similar across various methods. As a result, this metric may not be a sensitive evaluation criterion for this dataset.

Similarly, the METEOR metric considers synonyms and phrase reordering, emphasizing diverse matches of phrases and vocabulary. As indicated in Table III, VLCI achieves the best performance in terms of the METEOR metric on the IU-Xray dataset, but it falls short compared to MMTN on the MIMIC-CXR dataset. This suggests that there are some limitations in matching phrase and vocabulary diversity in our approach. By referring to Table I, we observe that both the best-performing MMTN and AlignTransformer benefit from knowledge supplementation and the assistance of a memory module, potentially enhancing the model’s ability to estimate synonyms more effectively. While our approach relies on learning semantics solely from the linear projection space of tokens, which may have limitations.

Moreover, CIDEr metrics emphasizes the importance of

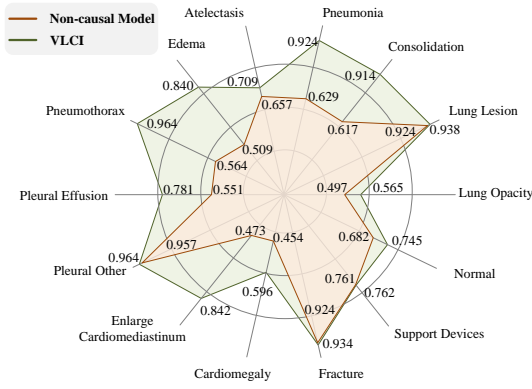


Fig. 6. Evaluation of abnormality classification results (accuracy) on MIMIC-CXR. The baseline model is the transformer without causal intervention.

more significant and information-rich words in the generated text, rather than common words, posing a challenge for long sequence reports containing medical terminology. on the MIMIC-CXR dataset, VLCI outperforms two open-source non-knowledge-based methods (R2Gen and R2GenCMN) but falls behind knowledge-based methods (PPKED, MGSK, DCL). We speculate that domain-specific knowledge with specialized concepts can assist the model in generating more accurate disease descriptions and achieving superior performance, even if these descriptions may be less common. Our VLCI focuses on causal intervention within cross-modal data without relying on external knowledge, making it unable to accurately capture domain-specific terminology.

2) *CE Metric*: The purpose of MRG is to alleviate the burden on medical professionals and provide precise diagnostic evidence. Therefore, the CE metric is more appropriate for evaluating the clinical significance of MRG methods compared to NLG metrics, as it specifically assesses the accuracy of abnormality classification. The CE metric is only applied to the MIMIC-CXR dataset because the label extractor (CheXpert) [78] is specially designed for MIMIC-CXR to obtain class labels. Compared with the lightweight R2Gen in Table III, VLCI demonstrates a remarkable improvement of 15.6% in Precision, 6.7% in Recall, and 12.5% in F1-Score. This validates that VLCI can provide a more accurate clinic diagnosis rather than merely generating fluent reports. Additionally, our VLCI outperforms the state-of-the-art method DCL in terms of Precision score and F1 score. Notably, when compared to several knowledge-based methods, our approach achieves a more efficient clinical evidence generation by relying solely on causal intervention without requiring additional knowledge assistance. Nevertheless, the Recall score is relatively lower compared to M2TR in Table III, indicating that the dataset may contain extreme categories. M2TR employs staged generation, which leverages the preliminary concepts generated in the first stage, enabling effective anomaly detection. However, this process can also lead to an increase in false positives, consequently reducing the Precision score.

C. Qualitative Analysis

To further validate the assistance of causal intervention (i.e., alleviate the burden on medical professionals and provide precise diagnostic evidence) in our method, we extract 14

categories of labels from the reports generated by the baseline and VLCI, and evaluated their accuracy, as shown in Fig. 6. Our approach achieves significant performance improvements in all categories, particularly in “Edema” (0.509 \rightarrow 0.840) and “Enlarge Cardiomegastinum” (0.473 \rightarrow 0.842). This is because our VLCI explores sufficient visual information and further produces more accurate and less biased descriptions by cross-modal causal intervention than the Transformer baseline. However, the estimation of some categories remains ambiguous, e.g., “Lung Opacity”. It reveals that VLCI can provide a comprehensive consideration of various radiologic signs to detect the abnormality but give less improvement for the single source abnormality. For example, whether “Edema” is caused by the heart has different radiologic signs, while the increase in lung density can be considered as “Lung Opacity”. Thus, VLCI can capture the abnormality with complex causes more effectively, where exists more spurious correlations. Besides, Fig. 6 shows the unavailability of causal intervention in independent abnormalities, e.g. “Support Devices”.

We further conduct the qualitative analysis on the MIMIC-CXR dataset via three intuitive generated examples of the baseline and the VLCI in Fig. 7. In Fig. 7 (a), the reference report contains three abnormalities. However, the baseline model neglects “pleural effusion” and “consolidation,” while VLCI accurately identifies all abnormalities. This indicates that our VDM comprehensively captures all essential visual features, crucial for MRG. Fig. 7 (b) shows an example where the same visual region is simultaneously discovered by the baseline and the VLCI but leads to different descriptions. Our VLCI can accurately describe the heart, while the baseline is uncertain and even has a miscalculation of pneumonia. It shows that LDM can alleviate the semantic bias caused by word frequency in word embedding space. Fig. 7 (c) illustrates a complex causal graph, where “atelectasis” and “edema” could also be causes of “cardiomegaly.” However, the baseline fails to correctly consider the causes of “cardiomegaly” and erroneously captures these pieces of evidence. In contrast, VLCI leverages the causal intervention module to disentangle these confounders, enabling careful consideration of various pieces of evidence for an accurate judgment.

In Fig. 7 (d), the ground truth indicates the presence of hydropneumothorax, a condition characterized by the simultaneous presence of gas and fluid in the chest, whereas pleural effusion contains only fluid. Although VLCI correctly identifies the presence of gas and fluid in the chest, leading to the diagnosis of pneumothorax, it erroneously estimates pleural effusion due to insufficient relevant knowledge. In this example, our method produces inaccurate text and fails to identify pneumonia and lung consolidation. Moreover, while VDM and LDM excel at recognizing visual and language concepts, detecting highly specialized concepts with latent relations not explicitly present in the data presents challenges.

D. Ablation Studies

1) *effectiveness of VLCI*: In Table IV, we adopt the same setting as ResNet101 to conduct the ablation experiments using DenseNet121 as the backbone. We perform VLP and

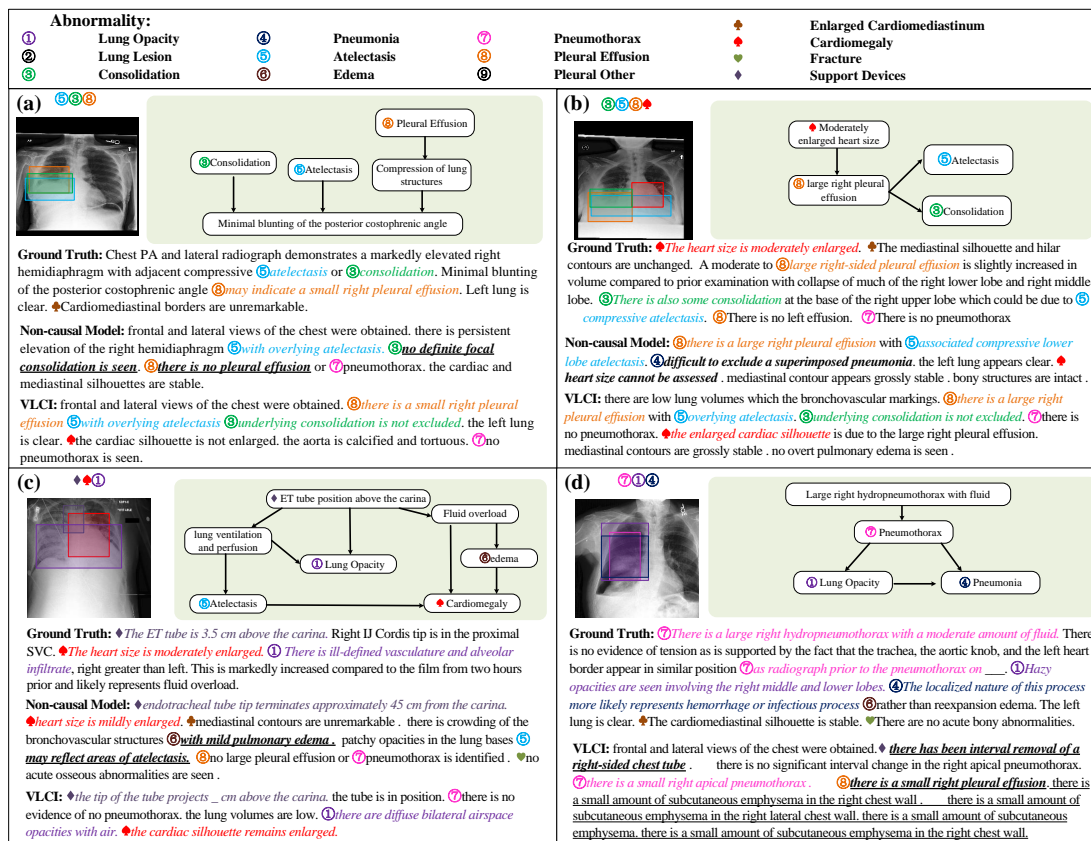


Fig. 7. The results of the Non-causal Model (Baseline) and VLCI models on the MIMIC-CXR dataset are presented in (a-c), and (d) shows the false sample in VLCI. Thirteen kinds of abnormalities are marked with different markers and colors. Note that keywords in the reports are also marked with different markers and colors. Correctly identified abnormalities are marked in the corresponding color, while other descriptions in bold, italics, and underscores are incorrect. Descriptions marked only with underscores indicate repeated words. In each sample, the green regions represent causal graphs constructed by ChatGPT based on Ground Truth, which can further elucidate the inherent causal relation within each example.

fine-tuning with causal intervention on IU-Xray and MIMIC-CXR datasets. Due to the small scale of the IU-Xray dataset and the simplicity of report content, the persuasiveness of the CIDEr metric on this dataset is limited. We evaluated BLEU-4, Rouge-L, and METEOR on the IU-Xray dataset, and the results indicate that our method still achieves a significant improvement with DenseNet121. However, we observed that the performance of models using DenseNet121 as the backbone is notably inferior to those using ResNet101. We speculate that while DenseNet121 is efficient in feature extraction due to its dense connections, it may not always provide the best performance for tasks involving specific types of medical images or requiring deeper feature extraction capabilities. Additionally, we conducted experiments on the larger MIMIC-CXR dataset, using BLEU-4, CIDEr, and METEOR as evaluation metrics. The experimental results further confirm our speculations and validate the effectiveness of our approach.

2) *Effectiveness of VLP:* In Table V, we conduct ablation experiments to assess the impact of masking ratios on model performance, and the results are presented. Our VLP model achieved the best performance with a higher masking ratio of 85%, which is in contrast to the optimal masking ratio of 75% reported by MAE [57]. We attribute this difference to the cross-modal information correlations, where the masked information can be reconstructed by visible features from both language and images. Furthermore, VLP tends to learn general

Method on IU-Xray	BLEU-4	Rouge-L	METEOR
ResNet101	0.148	0.345	0.180
ResNet101 + VLCI	0.190 (+0.042)	0.394 (+0.049)	0.210 (+0.03)
DenseNet121	0.164	0.361	0.183
DenseNet121 + VLCI	0.176 (+0.012)	0.394 (+0.033)	0.195 (+0.012)
Method on MIMIC-CXR	BLEU-4	CIDEr	METEOR
ResNet101	0.101	0.130	0.135
ResNet101 + VLCI	0.119 (+0.018)	0.190 (+0.06)	0.150 (+0.015)
DenseNet121	0.091	0.111	0.127
DenseNet121 + VLCI	0.113 (+0.022)	0.134 (+0.023)	0.149 (+0.022)

TABLE V
WE EVALUATED THE PERFORMANCE OF VARIOUS MASKING RATIOS FOR MIM ON THE IU-XRAY DATASET. WE PRE-TRAINED THE VLP MODEL FOR 100 EPOCHS AND THEN FINE-TUNED IT IN THE BASELINE (NON-CAUSAL MODEL) FOR AN ADDITIONAL 5 EPOCHS.

Masking Ratio	BLEU-1	BLEU-4	CIDEr	Rouge-L
Baseline	0.433	0.148	0.501	0.345
w/ 75%	0.450	0.160	0.486	0.360
w/ 85%	0.452	0.161	0.522	0.351
w/ 95%	0.432	0.153	0.460	0.346

features from the masked modality at higher masking ratios, while distinguishable features can be extracted by the complete information from another modality. To explore whether increasing the masking ratio further would further improve the performance, we experimented with a higher masking ratio of 95%. However, the decreased results in Table V indicate that this approach leads to excessive information loss.

TABLE VI

THE PERFORMANCE OF DIFFERENT PRE-TRAINING METHODS ON IU-XRAY, THE RESULT MARKED BY * MEANS FINE-TUNING WITH 10 EPOCHS, WHILE THE REST ONLY USE THE ENCODER WITH 100 EPOCHS. THE RESULT MARKED BY † IS FROM [79].

Method	BLEU-4	CIDEr	Rouge-L
Baseline	0.148	0.501	0.345
w/ MAE	0.154	0.486	0.360
w/ VisualGPT†	0.159	0.497	0.374
w/ VLP (MIM)	0.162	<u>0.602</u>	0.362
w/ VLP (PLM)	<u>0.165</u>	0.538	<u>0.365</u>
w/ VLP (PLM+MIM)	0.160	0.431	0.364
w/ VLP (PLM)*	0.151	0.399	0.349
w/ VLP (PLM+MIM)*	0.161	0.522	0.351
w/ VLP (PLM+MIM+Degradation)* (Ours)	0.170	0.631	0.363

TABLE VII

ABLATION ANALYSIS OF OUR VLCI. THE BASELINE IS IMPLEMENTED BY THE TRANSFORMER. THE MARKER AT THE BASELINE (NON-CAUSAL MODEL) AND R2Gen [5] MEANS THE OPERATION IN THE BRACKETS.

Dataset	Method	BLEU-4	CIDEr	Rouge-L	
IU-Xray	Baseline	0.148	0.501	0.345	
	Baseline ^{w♦} (w/ VDM)	0.160	0.521	0.364	
	Baseline ^{w•} (w/ LDM)	0.155	0.509	0.361	
	Baseline ^{w♦•} (w/ VDM&LDM)	0.163	0.544	0.361	
	R2Gen	0.165	0.493	0.360	
	R2Gen ^{w♦} (w/ VDM)	0.171	0.553	0.370	
	R2Gen ^{w•} (w/ LDM)	0.166	0.546	0.360	
	R2Gen ^{w♦•} (w/ VDM&LDM)	0.173	<u>0.628</u>	0.368	
	Baseline ^{w★} (w/ VLP)	0.170	0.631	0.363	
	Baseline ^{w♦★} (w/ VLP&VDM)	0.174	0.523	0.374	
	Baseline ^{w•★} (w/ VLP&LDM)	0.178	0.573	0.378	
	VLCI	0.190	0.592	0.394	
	MIMIC-CXR	Baseline	0.101	0.130	0.270
		Baseline ^{w♦} (w/ VDM)	0.103	0.144	0.272
Baseline ^{w•} (w/ LDM)		0.069	0.071	0.224	
Baseline ^{w♦•} (w/ VDM&LDM)		0.070	0.074	0.230	
R2Gen		0.103	0.168	<u>0.278</u>	
R2Gen ^{w♦} (w/ VDM)		0.106	0.171	0.277	
R2Gen ^{w•} (w/ LDM)		0.091	0.136	0.256	
R2Gen ^{w♦•} (w/ VDM&LDM)		0.100	0.143	0.264	
Baseline ^{w★} (w/ VLP)		0.106	0.151	<u>0.278</u>	
Baseline ^{w♦★} (w/ VLP&VDM)		0.110	<u>0.177</u>	0.280	
Baseline ^{w•★} (w/ VLP&LDM)		<u>0.115</u>	0.157	0.277	
VLCI		0.119	0.190	0.280	

In Table VI, we make a comparison with different pre-training methods. It shows that the cross-modal pre-training method has a more robust representation ability than the MIM with single-modality. However, the Rouge-L metric in VisualGPT surpasses ours, possibly due to its exclusive pre-training of the text decoder, enabling more concentrated learning of the intricate structure in medical reports. Additionally, our cross-modal pre-training achieves comparable performance to the PLM model that only fine-tunes the encoder, while ours fine-tunes the whole model with fewer epochs. Moreover, our VLP adopts the degradation images as input, which facilitates the extraction of visual details in the downstream task.

Furthermore, in Table VII, Baseline^{w♦•} is significantly worse than baseline on the MIMIC-CXR dataset, e.g., 0.101 \rightarrow 0.070 for BLEU-4, while still keeping performance improvement on IU-Xray dataset. This validates the significant feature complexity from the large-scale MIMIC-CXR dataset leads to unstable probability distribution estimation with causal intervention. Meanwhile, we find that the VLP can substantially boost the performance of the baseline, e.g.,

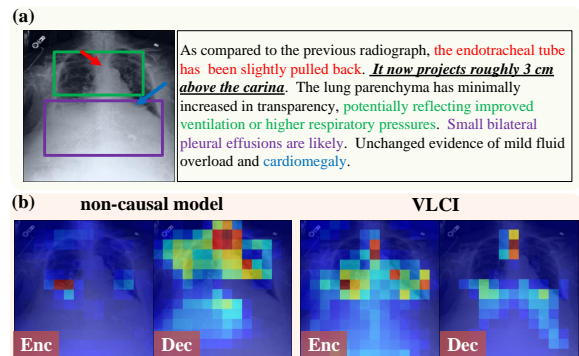


Fig. 8. The visualization of the attention map. (a) is an example from the MIMIC-CXR dataset that the colored text should be discovered in the marked region of the image. The images in (b) are the attention maps of the non-causal model and our VLCI, respectively. The tag “Enc” means the accumulated attention maps from the encoder for the selected local features, and “Dec” is the response to the “pleural” (decoder output).

0.148 \rightarrow 0.170, 0.101 \rightarrow 0.106 for BLEU-4 on IU-Xray and MIMIC-CXR datasets, respectively. The improvement is caused by the learned comprehensive concepts and context in the pre-training and the cross-modal features alignment stage, which shows the importance of VLP. Similarly, The Rough-L is also barely improved due to the features’ complexity and long sequence from the MIMIC-CXR dataset. For example, although AlignTransformer achieves the same score of the Rough-L as CA on the MIMIC-CXR, it outperforms CA on all other metrics.

3) *Effectiveness of Causal Intervention: VDM.* In Table VII, Baseline^{w♦} and R2Gen^{w♦} can boost the performance compared to Baseline and R2Gen, which demonstrates the validity of the VDM. However, the improvement of BLEU-4 between Baseline^{w♦★} and Baseline^{w★} on the IU-Xray dataset is more significant than that on the MIMIC-CXR dataset. This is because the VDM can discover essential visual information, but the report of the MIMIC-CXR is more complex and the model fails to generate accurate descriptions. The performance degradation of CIDEr can further illustrate it.

In Fig. 8, the encoder of the non-causal model exhibits limited attention to all potential abnormal regions. Instead, it excessively focuses on the base of the lung, possibly due to the dataset’s high prevalence of lung-related diseases. In contrast, the attention map from the VLCI encoder can truly focus on the dominant regions that may indicate abnormalities, including the entire lung lobe, carina, and pleura, rather than false correlations with biased visual concepts. This confirms the semantic sensitivity of the VDM, which captures dominant visual content by performing visual causal interventions.

LDM. Compared to the VDM, the LDM plays a more significant role in MRG because the sophisticated linguistic semantic patterns within reports are entangled and biased that require elaborate linguistic deconfounding. In Table VII, the performance drops without LDM, e.g., 0.119 \rightarrow 0.110 for the BLEU-4 metric on the MIMIC-CXR dataset. This shows the importance of adjusting semantic relevance in word embedding space. Compared with the baseline, the performance improvement of Baseline^{w•★} on the MIMIC-CXR dataset demonstrates that the LDM can generate more accurate reports even with biased visual information. However, the CIDEr

metric on the IU-Xray dataset shows the effectiveness of the combination of VDM and LDM, while ILVD obtains a lower score. This is due to the worse diversity on the IU-Xray dataset, where Baseline^{w♦♦} and R2Gen^{w♦♦} can get higher CIDEr but lower BLEU-4 with inadequate multi-modal feature correlation. In Fig. 8 (b), the attention map of the decoder in the non-causal model exhibits evident redundant responses, with high attention widely distributed in the upper part of the lung, especially the carina. The VLCI, in contrast, can capture dominant semantic information in a coarse-to-fine manner, refining it from the potential abnormal regions that receive extensive attention in the encoder to the bilateral thorax. The high attention on the carina may be attributed to the presence of a support device that could increase cardiac load, cause vascular occlusion or congestion, leading to changes in intrathoracic pressure and eventually resulting in pleural effusion. These findings indicate that the LDM can capture more discriminative semantic information from the linguistic modality through linguistic front-door interventions.

V. CONCLUSION

In this paper, we propose Visual-Linguistic Causal Intervention (VLCI) framework for MRG, to implicitly deconfound the visual-linguistic confounders by causal front-door intervention. To alleviate the problem of unpaired visual-linguistic data when pre-training, we combine the PLM and MIM for cross-modal pre-training. To implicitly mitigate cross-modal confounders and discover the true cross-modal causality, we propose visual-linguistic causal front-door intervention modules VDM and LDM. Experiments on IU-Xray and MIMIC-CXR datasets show that our VLCI can effectively mitigate visual-linguistic bias and outperforms the state-of-the-art methods. The lower computational cost and faster inference speed of VLCI promote its clinical application. In the future work, we will distill medical knowledge from large language models (LLMs) for more medical imaging modalities such as CT, MRI, and pathological slides. We believe our work could inspire more causal reasoning methods in MRG.

REFERENCES

- [1] Q. Yu, L. Qi, Y. Gao, W. Wang, and Y. Shi, "Crosslink-net: double-branch encoder network via fusing vertical and horizontal convolutions for medical image segmentation," *IEEE Transactions on Image Processing*, vol. 31, pp. 5893–5908, 2022.
- [2] S. K. Zhou, H. Greenspan, C. Davatzikos, J. S. Duncan, B. Van Ginneken, A. Madabhushi, J. L. Prince, D. Rueckert, and R. M. Summers, "A review of deep learning in medical imaging: Imaging traits, technology trends, case studies with progress highlights, and future promises," *Proceedings of the IEEE*, vol. 109, no. 5, pp. 820–838, 2021.
- [3] T. Tanida, P. Müller, G. Kaissis, and D. Rueckert, "Interactive and explainable region-guided radiology report generation," in *Proceedings of the IEEE/CVF Conference on Computer Vision and Pattern Recognition*, 2023, pp. 7433–7442.
- [4] T.-S. Nguyen and B. Fernando, "Effective multimodal encoding for image paragraph captioning," *IEEE Transactions on Image Processing*, vol. 31, pp. 6381–6395, 2022.
- [5] Z. Chen, Y. Song, T.-H. Chang, and X. Wan, "Generating radiology reports via memory-driven transformer," in *Proceedings of the 2020 Conference on Empirical Methods in Natural Language Processing (EMNLP)*, 2020, pp. 1439–1449.
- [6] Y. Zhang, X. Wang, Z. Xu, Q. Yu, A. Yuille, and D. Xu, "When radiology report generation meets knowledge graph," in *Proceedings of the AAAI Conference on Artificial Intelligence*, vol. 34, no. 07, 2020, pp. 12910–12917.
- [7] F. Liu, X. Wu, S. Ge, W. Fan, and Y. Zou, "Exploring and distilling posterior and prior knowledge for radiology report generation," in *CVPR*, 2021, pp. 13 753–13 762.
- [8] F. Liu, C. Yin, X. Wu, S. Ge, P. Zhang, and X. Sun, "Contrastive attention for automatic chest x-ray report generation," in *Findings of the Association for Computational Linguistics: ACL-IJCNLP 2021*, 2021, pp. 269–280.
- [9] S. Yang, X. Wu, S. Ge, S. K. Zhou, and L. Xiao, "Knowledge matters: Chest radiology report generation with general and specific knowledge," *Medical Image Analysis*, p. 102510, 2022.
- [10] J. Pearl, M. Glymour, and N. P. Jewell, *Causal inference in statistics: A primer*. John Wiley & Sons, 2016.
- [11] Y. Liu, Y.-S. Wei, H. Yan, G.-B. Li, and L. Lin, "Causal reasoning meets visual representation learning: A prospective study," *Machine Intelligence Research*, pp. 1–27, 2022.
- [12] Z. Yue, H. Zhang, Q. Sun, and X.-S. Hua, "Interventional few-shot learning," *Advances in Neural Information Processing Systems*, vol. 33, 2020.
- [13] T. Wang, J. Huang, H. Zhang, and Q. Sun, "Visual commonsense representation learning via causal inference," in *CVPR Workshops*, 2020, pp. 378–379.
- [14] Y. Niu, K. Tang, H. Zhang, Z. Lu, X.-S. Hua, and J.-R. Wen, "Counterfactual vqa: A cause-effect look at language bias," in *Proceedings of the IEEE/CVF Conference on Computer Vision and Pattern Recognition*, 2021, pp. 12 700–12 710.
- [15] B. Liu, D. Wang, X. Yang, Y. Zhou, R. Yao, Z. Shao, and J. Zhao, "Show, deconfound and tell: Image captioning with causal inference," in *CVPR*, 2022, pp. 18 041–18 050.
- [16] Y. Liu, G. Li, and L. Lin, "Cross-modal causal relational reasoning for event-level visual question answering," *IEEE Transactions on Pattern Analysis and Machine Intelligence*, 2023.
- [17] X. Yang, H. Zhang, G. Qi, and J. Cai, "Causal attention for vision-language tasks," in *CVPR*, 2021, pp. 9847–9857.
- [18] X. Yang, H. Zhang, and J. Cai, "Deconfounded image captioning: A causal retrospect," *PAMI*, 2021.
- [19] J. Devlin, M.-W. Chang, K. Lee, and K. Toutanova, "Bert: Pre-training of deep bidirectional transformers for language understanding," *arXiv preprint arXiv:1810.04805*, 2018.
- [20] M. Stefanini, M. Cornia, L. Baraldi, S. Cascianelli, G. Fiameni, and R. Cucchiara, "From show to tell: a survey on deep learning-based image captioning," *PAMI*, 2022.
- [21] A. Karpathy and L. Fei-Fei, "Deep visual-semantic alignments for generating image descriptions," in *Proceedings of the IEEE conference on computer vision and pattern recognition*, 2015, pp. 3128–3137.
- [22] P. Anderson, X. He, C. Buehler, D. Teney, M. Johnson, S. Gould, and L. Zhang, "Bottom-up and top-down attention for image captioning and visual question answering," in *CVPR*, 2018, pp. 6077–6086.
- [23] N. Yu, X. Hu, B. Song, J. Yang, and J. Zhang, "Topic-oriented image captioning based on order-embedding," *IEEE Transactions on Image Processing*, vol. 28, no. 6, pp. 2743–2754, 2018.
- [24] W. Jiang, M. Zhu, Y. Fang, G. Shi, X. Zhao, and Y. Liu, "Visual cluster grounding for image captioning," *IEEE Transactions on Image Processing*, vol. 31, pp. 3920–3934, 2022.
- [25] Y. Wang, Z. Lin, X. Shen, S. Cohen, and G. W. Cottrell, "Skeleton key: Image captioning by skeleton-attribute decomposition," in *Proceedings of the IEEE conference on computer vision and pattern recognition*, 2017, pp. 7272–7281.
- [26] Y. Xian and Y. Tian, "Self-guiding multimodal lstm—when we do not have a perfect training dataset for image captioning," *IEEE Transactions on Image Processing*, vol. 28, no. 11, pp. 5241–5252, 2019.
- [27] A. Radford, K. Narasimhan, T. Salimans, I. Sutskever *et al.*, "Improving language understanding by generative pre-training," 2018.
- [28] V.-Q. Nguyen, M. Suganuma, and T. Okatani, "Grit: Faster and better image captioning transformer using dual visual features," in *ECCV*, 2022, pp. 167–184.
- [29] L. Zhou, Y. Zhang, Y.-G. Jiang, T. Zhang, and W. Fan, "Re-caption: Saliency-enhanced image captioning through two-phase learning," *IEEE Transactions on Image Processing*, vol. 29, pp. 694–709, 2019.
- [30] H. Liu, S. Zhang, K. Lin, J. Wen, J. Li, and X. Hu, "Vocabulary-wide credit assignment for training image captioning models," *IEEE Transactions on Image Processing*, vol. 30, pp. 2450–2460, 2021.
- [31] J. Yu, Z. Wang, V. Vasudevan, L. Yeung, M. Seyedhosseini, and Y. Wu, "Coca: Contrastive captioners are image-text foundation models," *arXiv preprint arXiv:2205.01917*, 2022.
- [32] Z. Wang, J. Yu, A. W. Yu, Z. Dai, Y. Tsvetkov, and Y. Cao, "SimVlm: Simple visual language model pretraining with weak supervision," *arXiv preprint arXiv:2108.10904*, 2021.

- [33] M. Glymour, J. Pearl, and N. P. Jewell, *Causal inference in statistics: A primer*. John Wiley & Sons, 2016.
- [34] J. Pearl and D. Mackenzie, *The book of why: the new science of cause and effect*. Basic books, 2018.
- [35] K. Tang, J. Huang, and H. Zhang, “Long-tailed classification by keeping the good and removing the bad momentum causal effect,” *Advances in Neural Information Processing Systems*, vol. 33, pp. 1513–1524, 2020.
- [36] C. Ouyang, C. Chen, S. Li, Z. Li, C. Qin, W. Bai, and D. Rueckert, “Causality-inspired single-source domain generalization for medical image segmentation,” *IEEE Transactions on Medical Imaging*, vol. 42, no. 4, pp. 1095–1106, 2022.
- [37] R. Liu, H. Liu, G. Li, H. Hou, T. Yu, and T. Yang, “Contextual debiasing for visual recognition with causal mechanisms,” in *Proceedings of the IEEE/CVF Conference on Computer Vision and Pattern Recognition*, 2022, pp. 12755–12765.
- [38] T. Wang, C. Zhou, Q. Sun, and H. Zhang, “Causal attention for unbiased visual recognition,” in *ICCV*, 2021, pp. 3091–3100.
- [39] C. Zang, H. Wang, M. Pei, and W. Liang, “Discovering the real association: Multimodal causal reasoning in video question answering,” in *Proceedings of the IEEE/CVF Conference on Computer Vision and Pattern Recognition*, 2023, pp. 19027–19036.
- [40] Z. Yang, M. Lin, X. Zhong, Y. Wu, and Z. Wang, “Good is bad: Causality inspired cloth-debiasing for cloth-changing person re-identification,” in *Proceedings of the IEEE/CVF Conference on Computer Vision and Pattern Recognition*, 2023, pp. 1472–1481.
- [41] Z. Hu and L. E. Li, “A causal lens for controllable text generation,” *Advances in Neural Information Processing Systems*, vol. 34, pp. 24941–24955, 2021.
- [42] D. Xue, S. Qian, and C. Xu, “Variational causal inference network for explanatory visual question answering,” in *Proceedings of the IEEE/CVF International Conference on Computer Vision*, 2023, pp. 2515–2525.
- [43] S. Zhao, M. Jiang, M. Liu, B. Qin, and T. Liu, “Causaltriad: toward pseudo causal relation discovery and hypotheses generation from medical text data,” in *Proceedings of the 2018 ACM international conference on bioinformatics, computational biology, and health informatics*, 2018, pp. 184–193.
- [44] J. Miao, C. Chen, F. Liu, H. Wei, and P.-A. Heng, “Causl: Causality-inspired semi-supervised learning for medical image segmentation,” in *Proceedings of the IEEE/CVF International Conference on Computer Vision*, 2023, pp. 21426–21437.
- [45] X. Li, X. Qian, L. Liang, L. Kong, Q. Dong, J. Chen, D. Liu, X. Yao, and Y. Fu, “Causally-aware intraoperative imputation for overall survival time prediction,” in *Proceedings of the IEEE/CVF Conference on Computer Vision and Pattern Recognition*, 2023, pp. 15681–15690.
- [46] Z. Huang, X. Zhang, and S. Zhang, “Kiut: Knowledge-injected u-transformer for radiology report generation,” in *Proceedings of the IEEE/CVF Conference on Computer Vision and Pattern Recognition*, 2023, pp. 19809–19818.
- [47] L. Wang, M. Ning, D. Lu, D. Wei, Y. Zheng, and J. Chen, “An inclusive task-aware framework for radiology report generation,” in *International Conference on Medical Image Computing and Computer-Assisted Intervention*. Springer, 2022, pp. 568–577.
- [48] M. Li, B. Lin, Z. Chen, H. Lin, X. Liang, and X. Chang, “Dynamic graph enhanced contrastive learning for chest x-ray report generation,” in *Proceedings of the IEEE/CVF Conference on Computer Vision and Pattern Recognition*, 2023, pp. 3334–3343.
- [49] S. Jain, A. Agrawal, A. Saporta, S. Q. Truong, D. N. Duong, T. Bui, P. Chambon, Y. Zhang, M. P. Lungren, A. Y. Ng *et al.*, “Radgraph: Extracting clinical entities and relations from radiology reports,” *arXiv preprint arXiv:2106.14463*, 2021.
- [50] D. You, F. Liu, S. Ge, X. Xie, J. Zhang, and X. Wu, “Aligntransformer: Hierarchical alignment of visual regions and disease tags for medical report generation,” in *MICCAI*. Springer, 2021, pp. 72–82.
- [51] J. Wang, A. Bhalerao, and Y. He, “Cross-modal prototype driven network for radiology report generation,” in *European Conference on Computer Vision*. Springer, 2022, pp. 563–579.
- [52] F. Liu, S. Ge, and X. Wu, “Competence-based multimodal curriculum learning for medical report generation,” *arXiv preprint arXiv:2206.14579*, 2022.
- [53] F. Nooralahzadeh, N. P. Gonzalez, T. Frauenfelder, K. Fujimoto, and M. Krauthammer, “Progressive transformer-based generation of radiology reports,” *arXiv preprint arXiv:2102.09777*, 2021.
- [54] Z. Wang, M. Tang, L. Wang, X. Li, and L. Zhou, “A medical semantic-assisted transformer for radiographic report generation,” in *MICCAI*. Springer, 2022, pp. 655–664.
- [55] Z. Chen, Y. Shen, Y. Song, and X. Wan, “Cross-modal memory networks for radiology report generation,” *arXiv preprint arXiv:2204.13258*, 2022.
- [56] Y. Zeng, X. Zhang, and H. Li, “Multi-grained vision language pre-training: Aligning texts with visual concepts,” *arXiv preprint arXiv:2111.08276*, 2021.
- [57] K. He, X. Chen, S. Xie, Y. Li, P. Dollár, and R. Girshick, “Masked autoencoders are scalable vision learners,” in *CVPR*, 2022, pp. 16000–16009.
- [58] W. Wang, H. Bao, L. Dong, J. Bjorck, Z. Peng, Q. Liu, K. Aggarwal, O. K. Mohammed, S. Singhal, S. Som *et al.*, “Image as a foreign language: Beit pretraining for all vision and vision-language tasks,” *arXiv preprint arXiv:2208.10442*, 2022.
- [59] K. He, X. Zhang, S. Ren, and J. Sun, “Deep residual learning for image recognition,” in *CVPR*, 2016, pp. 770–778.
- [60] X. Geng, H. Liu, L. Lee, D. Schuurams, S. Levine, and P. Abbeel, “Multimodal masked autoencoders learn transferable representations,” *arXiv preprint arXiv:2205.14204*, 2022.
- [61] H.-Y. Zhou, C. Lian, L. Wang, and Y. Yu, “Advancing radiograph representation learning with masked record modeling,” *arXiv preprint arXiv:2301.13155*, 2023.
- [62] Y. Seo, D. Hafner, H. Liu, F. Liu, S. James, K. Lee, and P. Abbeel, “Masked world models for visual control,” *arXiv preprint arXiv:2206.14244*, 2022.
- [63] D. Lopez-Paz, R. Nishihara, S. Chintala, B. Scholkopf, and L. Bottou, “Discovering causal signals in images,” in *CVPR*, 2017, pp. 6979–6987.
- [64] J. Qi, Y. Niu, J. Huang, and H. Zhang, “Two causal principles for improving visual dialog,” in *CVPR*, 2020, pp. 10860–10869.
- [65] K. Xu, J. Ba, R. Kiros, K. Cho, A. Courville, R. Salakhudinov, R. Zemel, and Y. Bengio, “Show, attend and tell: Neural image caption generation with visual attention,” in *ICML*. PMLR, 2015, pp. 2048–2057.
- [66] J. Sun, D. Wei, L. Wang, and Y. Zheng, “Lesion guided explainable few weak-shot medical report generation,” in *International Conference on Medical Image Computing and Computer-Assisted Intervention*. Springer, 2022, pp. 615–625.
- [67] J. He, J.-N. Chen, S. Liu, A. Kortylewski, C. Yang, Y. Bai, and C. Wang, “Transfg: A transformer architecture for fine-grained recognition,” in *AAAI*, vol. 36, no. 1, 2022, pp. 852–860.
- [68] Z. Dai, H. Liu, Q. V. Le, and M. Tan, “Coatnet: Marrying convolution and attention for all data sizes,” *NeurIPS*, vol. 34, pp. 3965–3977, 2021.
- [69] B. Li, H. Zhou, J. He, M. Wang, Y. Yang, and L. Li, “On the sentence embeddings from pre-trained language models,” *arXiv preprint arXiv:2011.05864*, 2020.
- [70] Y. Cao, L. Cui, L. Zhang, F. Yu, Z. Li, and Y. Xu, “Mmtm: Multi-modal memory transformer network for image-report consistent medical report generation,” in *Proceedings of the AAAI Conference on Artificial Intelligence*, vol. 37, no. 1, 2023, pp. 277–285.
- [71] K. Zhang, H. Jiang, J. Zhang, Q. Huang, J. Fan, J. Yu, and W. Han, “Semi-supervised medical report generation via graph-guided hybrid feature consistency,” *IEEE Transactions on Multimedia*, 2023.
- [72] D. Demner-Fushman, M. D. Kohli, M. B. Rosenman, S. E. Shooshan, L. Rodriguez, S. Antani, G. R. Thoma, and C. J. McDonald, “Preparing a collection of radiology examinations for distribution and retrieval,” *Journal of the American Medical Informatics Association*, vol. 23, no. 2, pp. 304–310, 2015.
- [73] A. E. Johnson, T. J. Pollard, N. R. Greenbaum, M. P. Lungren, C.-y. Deng, Y. Peng, Z. Lu, R. G. Mark, S. J. Berkowitz, and S. Horng, “Mimic-cxr-jpg, a large publicly available database of labeled chest radiographs,” *arXiv preprint arXiv:1901.07042*, 2019.
- [74] K. Papineni, S. Roukos, T. Ward, and W.-J. Zhu, “Bleu: a method for automatic evaluation of machine translation,” in *ACL*, 2002, pp. 311–318.
- [75] L. C. ROUGE, “A package for automatic evaluation of summaries,” in *ACL*, 2004.
- [76] S. Banerjee and A. Lavie, “Meteor: An automatic metric for mt evaluation with improved correlation with human judgments,” in *Proceedings of the acl workshop on intrinsic and extrinsic evaluation measures for machine translation and/or summarization*, 2005, pp. 65–72.
- [77] R. Vedantam, C. Lawrence Zitnick, and D. Parikh, “Cider: Consensus-based image description evaluation,” in *CVPR*, 2015, pp. 4566–4575.
- [78] J. Irvin, P. Rajpurkar, M. Ko, Y. Yu, S. Ciurea-Illcus, C. Chute, H. Marklund, B. Haghgoo, R. Ball, K. Shpanskaya *et al.*, “Chexpert: A large chest radiograph dataset with uncertainty labels and expert comparison,” in *AAAI*, vol. 33, no. 01, 2019, pp. 590–597.
- [79] J. Chen, H. Guo, K. Yi, B. Li, and M. Elhoseiny, “Visualgpt: Data-efficient adaptation of pretrained language models for image captioning,” in *Proceedings of the IEEE/CVF Conference on Computer Vision and Pattern Recognition (CVPR)*, June 2022, pp. 18030–18040.



Weixing Chen has received the B.S. degree from the college of Medicine and Biological Information Engineering, Northeastern University, in 2020 and M.S. degree from Shenzhen Institute of Advanced Technology, Chinese Academy of Sciences in 2023. He is currently a research assistant at the School of Computer Science and Engineering, Sun Yat-sen University. His main interests include medical image analysis, multi-modal learning, and causal relation discovery. He has been serving as a reviewer for numerous academic journals and conferences.



Guanbin Li (M'15) is currently an associate professor in School of Computer Science and Engineering, Sun Yat-Sen University. He received his PhD degree from the University of Hong Kong in 2016. His current research interests include computer vision, image processing, and deep learning. He is a recipient of ICCV 2019 Best Paper Nomination Award. He has authorized and co-authored on more than 100 papers in top-tier academic journals and conferences. He serves as an area chair for the conference of VISAPP. He has been serving as a reviewer for numerous academic journals and conferences such as TPAMI, IJCV, TIP, TMM, TCyb, CVPR, ICCV, ECCV and NeurIPS.



Yang Liu (M'21) is currently a research associate professor working at the School of Computer Science and Engineering, Sun Yat-sen University. He received his Ph.D. degree from Xidian University in 2019. His current research interests include multi-modal cognitive reasoning and causal relation discovery. He is the recipient of the First Prize of the Third Guangdong Province Young Computer Science Academic Show. He has authorized and co-authored more than 20 papers in top-tier academic journals and conferences such as TPAMI, TIP, TCSVT, TII, CVPR, ICCV, IJCAI, and ACM MM. More information can be found on his personal website <https://yangliu9208.github.io>.



Ce Wang has received the B.S. degree from the Department of Mathematics, Jilin University, in 2015 and Ph.D. degree from the Center for Combinatorics, Nankai University in 2020. He is currently a postdoctoral researcher in the Institute of Computing Technology, Chinese Academy of Sciences. His main interests include generative modeling, image and video processing, computational imaging, medical image analysis, and explainable healthcare AI. He has been serving as a reviewer for numerous academic journals and conferences such as TMI, MIA, TCSVT, NIPS, ICLR, MICCAI, and ACM MM.



Liang Lin (M'09, SM'15) is a Full Professor of computer science at Sun Yat-sen University. He served as the Executive Director and Distinguished Scientist of SenseTime Group from 2016 to 2018, leading the R&D teams for cutting-edge technology transferring. He has authored or co-authored more than 200 papers in leading academic journals and conferences, and his papers have been cited by more than 29,000 times. He is an associate editor of IEEE Trans. Neural Networks and Learning Systems and IEEE Trans. Multimedia, and served as Area Chairs for numerous conferences such as CVPR, ICCV, SIGKDD and AAAI. He is the recipient of numerous awards and honors including Wu Wen-Jun Artificial Intelligence Award, the First Prize of China Society of Image and Graphics, ICCV Best Paper Nomination in 2019, Annual Best Paper Award by Pattern Recognition (Elsevier) in 2018, Best Paper Dimond Award in IEEE ICME 2017, Google Faculty Award in 2012. His supervised PhD students received ACM China Doctoral Dissertation Award, CCF Best Doctoral Dissertation and CAAI Best Doctoral Dissertation. He is a Fellow of IET/IAPR.



Jiarui Zhu is currently a Ph.D. student in Department of Health Technology and Informatics, the Hong Kong Polytechnic University. He received his master of science degree from the Hong Kong Polytechnic University in 2023. His current research interests include medical imaging processing and deep learning.



Shen Zhao received his Ph.D. degree in Tsinghua University in 2015. He is now researching on deep learning methods in medical image analysis. His research interests are mainly on automatic disease diagnosis on multi-model spinal images using novel methods on object detection/segmentation, metric learning, deep active contours, and the combination of visual and linguistic information in medical image diagnosis.